Visible Light-Driven H_2 Production over Highly Dispersed Ruthenia on Rutile TiO_2 Nanorods

Thuy-Duong Nguyen-Phan,[1] Si Luo,[1,2] Dimitriy Vovchok,[1,2] Jordi Llorca,[3] Jesús Graciani,[4] Shawn Sallis,[5] Wenqian Xu,[6] Jianming Bai,[7] Louis F. J. Piper,[5] Dmitry E. Polyansky,[1] Etsuko Fujita,[1] Sanjaya D. Senanayake,[1] Dario J. Stacchiola,[1] and José A. Rodriguez[1,2]**

[1] Chemistry Department, and [7] Photon Sciences Division, Brookhaven National Laboratory, Upton, NY 11973, US

[2] Department of Chemistry, Stony Brook University, Stony Brook, NY 11790, US

[3] Institute of Energy Technologies and Centre for Research in NanoEngineering, Universitat Politècnia de Catalunya, Diagonal 647, 08028 Barcelona, Spain

[4] Department of Physical Chemistry, University of Seville, E-41012, Seville, Spain

[5] Materials Science & Engineering, Department of Physics, Applied Physics and Astronomy, Binghamton University, Binghamton, NY 13902, US

[6] Advanced Photon Source, Argonne National Laboratory, Argonne, Illinois 60439, US

ABSTRACT

The immobilization of miniscule quantities of RuO_2 (~ 0.1%) onto one-dimensional (1D) TiO_2 nanorods (NRs) allows H_2 evolution from water under the irradiation of visible light. Rod-like rutile TiO_2 structures, exposing preferentially (110) surfaces, are shown to be critical for the deposition of RuO_2 to enable photocatalytic activity in the visible region. This performance is rationalized based on fundamental experimental studies and theoretical calculations, demonstrating that RuO_2(110) grown as 1D nanowires on rutile TiO_2(110), which occurs only at extremely low loads of RuO_2, leads to the formation of a hetero-interface that efficiently adsorbs visible light.

KEYWORDS

Titanium; Ruthenium; H_2 production; Water splitting; Heterojunction.

INTRODUCTION

Hydrogen obtained from carbon-free sources is an attractive alternative clean fuel that could potentially offer solutions to global warming through the reduction of CO_2 emissions. The splitting of water into H_2 and O_2 utilizing solar energy is regarded as one of the most promising and sustainable technologies to produce hydrogen.[1-3] Although titanium dioxide (TiO_2) is the most common semiconductor oxide photocatalyst,[3-6] its practical application is limited because TiO_2 absorbs only a small fraction of solar light and the photogenerated electrons/holes recombine rapidly.[4,5] Anchoring or coupling metal or metal oxide nanoparticles (NPs) onto TiO_2 has been used to either enhance its solar-conversion efficiency by retarding the charge carrier recombination or extending its response toward the visible light region stemming from band level alignment.[6,7] Precious metals possessing much larger work function than TiO_2,[6] such as Pt, Pd, Ru and Au, have been considered as the best candidates to suppress the charge carrier recombination and facilitate the charge transfer owing to the formation of Schottky barriers at the heterogeneous nanoscale junction and the localized surface plasmon resonance.[3,6,7] However, such a method of metallization is uneconomical if it demands large amounts of precious metals.

Since RuO_2 belongs to the class of *d*-band metallic conducting transition metal oxides, its electrical resistivity is two-fold higher than that of metallic ruthenium.[8] The intraband transitions and localized surface plasmon resonance of RuO_2 also play a vital role in its optical response and photoactivity.[9-11] Among several polymorphs of TiO_2, rutile is the thermodynamically most stable phase, but the moderate-temperature post treatment usually required to achieve highly crystalline rutile phase, results in large particle sizes and nonporosity.[6,5] Coupling rutile TiO_2 with RuO_2 has been widely studied in numerous catalytic reactions due to their lattice matching and strong metal-support interaction.[12-17] Seki[14] claimed that RuO_2/rutile-TiO_2 catalyst exhibited high catalytic activity and thermal stability

toward HCl oxidation to Cl_2 due to highly dispersed, ultrafine RuO_2 crystallites, approximately a single unit-cell thickness, that cover the surface of TiO_2 primary particle with strong interaction between RuO_2 and TiO_2. Xiang *et al.*[15] demonstrated that the re-distribution or spreading of RuO_2 occurred from a spherical shape (~ sub 2 nm) to epitaxial island layers along the TiO_2 surfaces during the chlorination reaction, forming a unique heterostructure at the interface. Lin *et al.*[17] elucidated that among several oxide supports including anatase TiO_2, rutile TiO_2, rutile SnO_2, Al_2O_3 and SiO_2, rutile TiO_2 was the most appropriate support to enhance the catalytic activity of N_2O reduction. Similarly, Jiao *et al.*[16] employed thermal treatment to transform RuO_2 nanoclusters (*ca.* 2 nm) into an epitaxial layer on the surface of both anatase and rutile TiO_2, relying on the interfacial atom arrangement match between these two oxides that led to more significant exposure of RuO_2 (110) facets and thus, promoting photocatalytic CO oxidation. Several key strategies are important including: choosing an appropriate support for highly dispersing metallic Ru or RuO_2 NPs to achieve optimal photocatalytic performance; improve the stability as well as decrease the amount of costly precursor being utilized but most notably, aim to preserve all specific properties of each component.

In spite of its promising catalytic features, very little attention has been paid so far concerning the explanation of the photocatalytic properties of the RuO_2/rutile-TiO_2 system. Most reported studies employed RuO_2 as a cocatalyst to facilitate the gas production under UV irradiation.[3,6,18-21] Recently, a first attempt toward H_2 production from water under UV excitation over RuO_2/anatase-TiO_2 nanocomposites was conducted, where an upward band bending at the RuO_2-TiO_2 interface has been proposed to explain the good performance of H_2 evolution.[21] In addition, density functional calculations performed on RuO_2/TiO_2(110) heterostructures for photocatalysis application found that the interface between RuO_2 and rutile TiO_2 strongly affects the atomic and electronic properties of both oxides due to a strong

charge accumulation at the interface.[22] Upward band bending at the interface could be observed when introducing oxygen vacancies at the interface and subsequently, the electron accumulation at the interface creates a strong internal electric field, leading to efficient separation of photoinduced electron-hole pairs during a photocatalytic process.[22] According to their calculation, the adsorption energy is lowered by 0.34 eV and the distance between H and bridging oxygen is shortened by 0.18 Å on $RuO_2/TiO_2(110)$ in comparison with that on $TiO_2(110)$ surface, therefore facilitating the splitting of water.

No attempt has been made to investigate the metal-support interaction between rutile RuO_2 and rutile TiO_2 support as well as to explain their photocatalytic properties in targeting H_2 production. We have synthesized a RuO_2/TiO_2 heterostructure by immobilizing minute quantities of RuO_2 onto 1D TiO_2 nanorods (NRs). Complementary characterization techniques have been applied to gain insight into the promotion effect of the heterostructure on the visible-light-responsive activity combined with DFT calculations of RuO_2 on rutile $TiO_2(110)$.

EXPERIMENTAL

Synthesis of RuO_2/TiO_2 heterostructures

All the chemicals were purchased from Aldrich and used without purification. Typically, a mixture of 7 mL of titanium n-butoxide and 7 mL of hydrochloric acid (35 wt%) was hydrothermally treated for 11 h at 105 °C. The white precipitate was carefully collected and washed several times with deionized water, thrice by aqueous 0.1 M NH_4OH solution, and finally with deionized water to entirely remove chlorine contaminants. After drying at 80 °C overnight, the blank TiO_2 rods (denoted as 'TiO_2') were obtained after calcined the *as-syn* TiO_2 rods in air at 200 °C for 2h.

Subsequently, 0.2 g of *as-syn* TiO_2 was re-dispersed in 20 mL of deionized water at 90 °C for 30 min. The impregnation of RuO_2 was carried out by drop-wise addition of an

appropriate concentration of 5 mL aqueous $RuCl_3.xH_2O$ solution at 90 °C. The fine powder after evaporation was sequentially washed with deionized water, aqueous 0.1 M NH_4OH solution, and deionized water to entirely remove chlorine contaminants, and collected by high-speed centrifugation (20000 rpm). The powder was dried at 80 °C overnight and then calcined in air at 200 °C for 2h, denoted as 'xRuTi' where x = 0.01, 0.1, 0.25, and 0.5 wt% of RuO_2. For comparison, bulk rutile TiO_2 particle was prepared by annealed commercial TiO_2 P25 (Degussa) at 800 °C for 4 h and named as 'TiO_2_p'.

Characterizations

Synchrotron X-ray powder diffraction (SXPD) patterns were collected at beamline 17-BM-B (λ = 0.72768 Å) of the Advanced Photon Source at Argonne National Laboratory. 5 mg of powder were loaded into a 0.9-mm-ID kapton capillary and two-dimensional diffraction patterns were collected by a Perkin Elmer amorphous silicon detector. The data acquisition was integrated by QXRD while the crystalline phase identification, composition and lattice parameters were subsequently analyzed by Rietveld refinement using TOPAS 4.1 program.

High-resolution transmission electron microscopy (HR-TEM) and scanning transmission electron microscopy (STEM) images were recorded on Tecnai G^2 F20 S-TWIN transmission electron microscope equipped with a field emission electron source. It was operated at 200 kV while the point-to-point resolution and the resolution between lines were 0.24 and 0.10 nm, respectively. The powder samples were deposited from alcohol suspensions onto holey-carbon Cu grids. Brunauer-Emmett-Teller (BET) specific surface areas were determined by N_2 adsorption/desorption at 77 K using an Altimira AMI-300ip instrument. The powders were degassed at 150 °C to remove all surface-adsorbed contaminants prior to measurements. High-resolution X-ray photoemission spectra (XPS) of Ti 2p, O 1s, Ru 3d and Ru 3p were recorded on a laboratory-based monochromated Al *K*α source with a hemispherical analyzer. The core-level and ultraviolet photoelectron spectra (UPS) were measured with a constant

pass energy of 23.5 eV, which corresponds to an instrumental resolution of 0.51 eV obtained from analyzing both the Au $4f_{7/2}$ and Fermi edge of Au foil.

Further characterization of the materials was also conducted using several techniques available at the Center for Functional Nanomaterials (CFN) at BNL. Raman spectroscopy was performed on a WiTec Alpha combination microscope at room temperature with 633 nm laser as an excitation source. UV-Vis diffuse reflectance (DRS) measurements were collected at room temperature by PerkinElmer Lambda 950 spectrometer equipped with an integrating sphere assembly.

Visible-light-driven H_2 production measurements

The photocatalytic hydrogen evolution was conducted in a closed gas circulation and evacuation system. Powder catalyst were suspended in aqueous methanol solution (20 vol%) in a sealed quartz cell. After evacuation and Ar purging several times, the reactor was side-irradiated by a 150 W Xenon arc lamp equipped with a $CuSO_4$ filter and 400 nm long pass filter (400 nm < λ < 625 nm) under magnetic stirring. The reaction temperature was maintained at 293 K by continuous water circulation. The evolved gases were determined by gas chromatography (GC Agilent 6890N) equipped with FID and TCD detectors using Ar as the carrier gas. Detailed experiment and calculation of apparent quantum efficiency is described in Supporting Information.

Computational methods

We built our theoretical model based on the previously published STM images of RuO_x supported on TiO_2(110) surface.[23] The nanostructured ruthenia on titania was modelled as follows: (*i*) TiO_2(110) surface consisted of four O-Ti-O three-layers, keeping the two of the bottom fixed at the optimized bulk positions, allowing a vacuum region of 15 Å between repeated slabs; (*ii*) in order to achieve an isolated wire-like RuO_2(110) nanostructure a (3x1) and (3x6) surface models of the titania support were used for optics calculation and density of

states respectively; (*iii*) a full-relaxed three atomic layer width (O-Ru-O) wire was coupled to the titania support according to Yang *et al.*'s report[23]. We performed periodic DFT calculations using the Perdew-Wang 91 (PW91) functional[24] for the exchange-correlation potential. The effect of the core electrons on the valence states was represented with the projector-augmented wave (PAW) approach,[25] as implemented in the Vienna *ab-initio* simulation package (VASP 5.3),[26,27] with the valence states defined for each atom as Ti(3*s*,3*p*,3*d*,4*s*), Ru(4*s*,4*p*,4*d*,5*s*) and O(2*s*,2*p*) electrons, while the remaining electrons were kept frozen as core states. The valence electronic states are expanded in a basis of plane waves with a cutoff of 400 eV for the kinetic energy. In order to account for eventual reduction of the titania support (occupation of the Ti 3*d* states) a Hubbard-like U term was used, (GGA+U), according to the Dudarev *et al.*'s implementation,[28] which makes use of an effective parameter U_{eff}. We took a value U_{eff} = 4.5 eV satisfactorily used in our previous work dealing with supported cerium oxide particles on titania.[29] Calculations were performed at the Γ point of the Brillouin zone for the (3x6) surface model and with a 1x4x1 k-points grid for the (3x1) model.

RESULTS AND DISCUSSION

Visible-light-responsive H_2 production over RuO_2/TiO_2 heterostructures

Figure 1 shows the visible light-driven hydrogen production performance of xRuTi heterostructured photocatalysts as a function of RuO_2 content. The time profiles in **Figure 1A** demonstrates the stable, constant amounts of H_2 produced over all the rod-like RuO_2/TiO_2 heterostructured photocatalysts under the irradiation of visible light (400 nm < λ < 625 nm). Bulk rutile TiO_2 particle (TiO_2_p sample) is completely inactive for H_2 production with visible light irradiation, while TiO_2 nanorods present a moderate activity, producing 33 μmol of H_2 gas per gram catalyst per hour. This observation is consistent with recent report that sub-10 nm rutile NPs exhibited a significant improvement in photocatalytic activity for

visible-light-driven water splitting compared to the bulk oxide.[30] It is worth noting that the deposition of RuO_2 onto TiO_2 rods significantly enhances the H_2 evolution efficiency regardless of RuO_2 loading amount. As seen in **Figure 1B**, the activity trend follows a volcano shape where the mass-normalized rate of H_2 production over all xRuTi heterostructure materials is significantly higher than that over TiO_2 NRs with an optimal RuO_2 content of 0.1 wt% (425 μmol g^{-1} h^{-1}). The photocatalytic performance under full UV-visible irradiation (310-625 nm) followed the same trend, as shown in **Figure S1** (Supporting Information). The activities normalized to specific surface areas and apparent quantum efficiencies are summarized in Table 1. The apparent quantum efficiencies over supported RuO_2 are 4- to 12-times larger than that with TiO_2 NRs alone. It is observed that increasing RuO_2 loading amount to 0.25 and 0.5 wt% gradually decreases the H_2 evolved rate regardless of light excitation source. This remarkable result is compared to the case of Pt, which is extensively used as a co-catalyst on TiO_2. As shown in **Figure S2** (Supporting Information), upon the UV irradiation, the H_2 evolution activity over our Ru-based heterostructured photocatalyst is comparable to the platinized TiO_2 NRs prepared by *in situ* photodeposition method. However, Pt does not give activity at all in the visible light region. A few studies have reported visible-light-driven photocatalytic activity over RuO_2/TiO_2 nanocomposites.[31,32] Ismail *et al.*[31] reported that the visible-light photoactivity enhancement toward methanol oxidation was ascribed to the incorporation of a small amount of Ru^{4+} into the anatase lattice and the formation of some structural defects on the surface, facilitating the interfacial charge transfer of electrons/holes, whereas the addition of RuO_2 suppressed the UV-photonic efficiency of TiO_2.

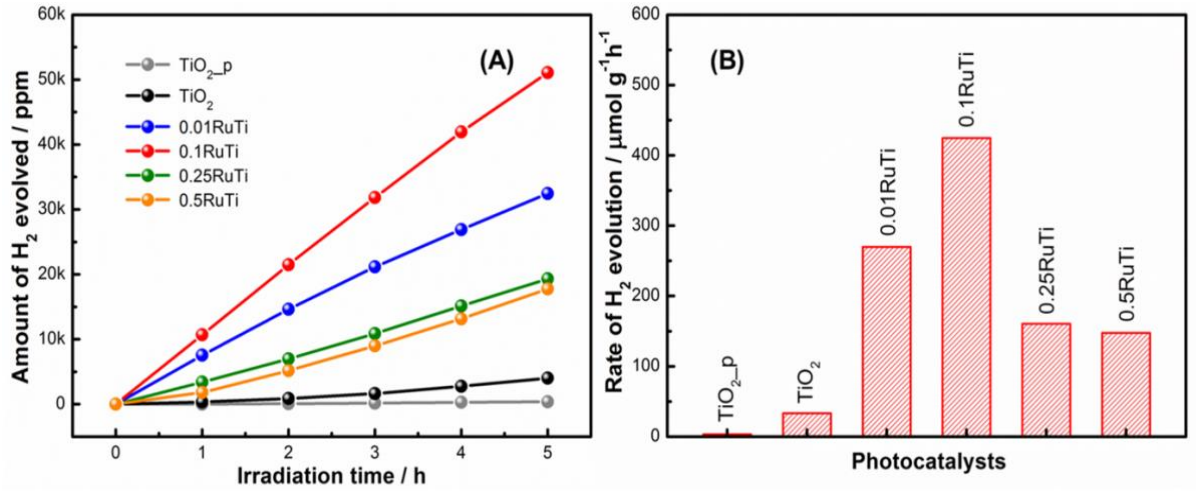

Figure 1. (A) Time profiles and (B) mass-normalized H_2 evolution rates over bulk TiO_2 particles, TiO_2 NRs and xRuTi heterostructures under Vis light illumination (400 – 625 nm).

Table 1. Surface areas, band gap energy, H_2 production rates and apparent quantum efficiencies over blank TiO_2 NRs and xRuTi heterostructures.

Samples	Surface area / m^2 g^{-1}	Band gap / eV [a]	H_2 production rate, r				AQE / % [d]	
			r_M [b]	r_S [c]	r_M' [b]	r_S' [c]	310-625 nm	400-625 nm
TiO_2	68	3.06	385	6	33	0.5	0.02	0.003
0.01RuTi	95	3.02	2001	21	270	2.8	0.12	0.024
0.1RuTi	90	2.99	3308	37	425	4.7	0.19	0.037
0.25RuTi	88	2.96	2714	31	160	1.8	0.16	0.014
0.5RuTi	81	2.93	2208	27	148	1.8	0.13	0.013

[a] Estimated from Tauc's plot of UV-Vis-DRS spectra.

[b] r_M, r_M'- Rates normalized to mass of photocatalyst, μmol g^{-1} h^{-1}, under UV-Vis and visible light irradiations, respectively.

[c] r_S, r_S'- Rates normalized to BET surface area, μmol m^2 h^{-1}, under UV-Vis and visible light irradiations, respectively.

[d] AQE - Apparent quantum efficiencies under UV-Vis and visible light irradiations, respectively.

We show here that 0.1 wt% of RuO_2 is the optimal loading amount onto TiO_2 NRs to reach the best photocatalytic performance for evolution of H_2, and also in the case of using TiO_2 particles as a substrate as displayed in **Figure S3** (Supporting Information). Excess RuO_2 loading (> 0.1 wt%) may detrimentally occupy the catalytically active sites on the surface of the photocatalyst, which can lead to a reduction of surface area as shown in **Table 1**. Furthermore, it may reduce the light penetration, retarding the activation of TiO_2 and the generation of photoinduced charge carriers and therefore diminishing the H_2 production. In a similar demonstration, Amama *et al.*[33] found that depositing beyond 0.4 wt% RuO_2 on TiO_2-glass fiber cotton significantly decreased the conversion of trichloroethylene oxidation. Similarly, the photonic efficiency for the methanol oxidation to HCHO reached a maximum at 0.5 wt% RuO_2-TiO_2 nanocomposite under visible light irradiation and further increasing up to 10 wt% gradually decreased the efficiency.[31] Much lower optimal contents, 0.05, 0.1, and 0.02 wt% of epitaxial RuO_2 layers, were obtained for P25, commercial anatase and commercial rutile TiO_2, respectively, in the RuO_2/TiO_2/Pt ternary photocatalyst for CO oxidation.[16] Lin *et al.*[34] also observed that loading less than 0.05 wt% RuO_2 on TiO_2 gave much higher activity toward the photocatalytic oxidation of sulfur-containing organic compounds and dyes. Sakata *et al.*[19] claimed that so small an amount of RuO_2, approximately 0.03 monolayer, on bulk TiO_2 surface (particle size of 0.2-0.4 μm, surface area of 10 m^2 g^{-1}) is sufficient to produce good photocatalytic activity of H_2 evolution. Excess amount can function as recombination centers because the distance between particles becomes shorter than the distance in which the image force to both electrons and holes is effective.[19] However, different conclusions have been reported by several groups, where 1 ~ 5 wt% of RuO_2 has been suggested to provide the best performance.[21,35] It can be concluded that optimizing the spatial distribution of RuO_2 loading on rutile TiO_2 support strongly depends on the synthesis method, support nature and experimental conditions. It is critical to develop

a synthesis method that allows the isolation of small amounts of RuO_2 on TiO_2. In the present work, miniscule quantity of RuO_2 gave the optimum photocatalytic H_2 production activity over both UV and visible light illuminations.

Structure-photoactivity correlation over RuO_2/TiO_2 heterostrutures

The crystallographic structure of TiO_2 NRs and xRuTi heterostructures obtained by X-ray diffraction are shown in **Figure 2A**. It is observed that the SXPD patterns were unchanged before and after RuO_2 addition onto TiO_2 NRs. Series of well-defined (110), (101), (111) and (211) diffraction peaks at 2θ = 12.9, 16.8, 19.1 and 24.9° were observed for all samples, indicating the dominance of tetragonal rutile phase (space group $P4_2/mnm$). The phase composition and cell parameters obtained from Rietveld refinement (**Figure S4**, Supporting Information) are summarized in **Table 2**. A small fraction of anatase (space group $I4_1/amd$) is observed as a single peak at 11.9°, occupying 7 ~ 11 wt%. No diffraction features related to the formation of RuO_2 particles are observed, possibly due to the high dispersion of ultrafine, small RuO_2 NPs, and/or the epitaxial growth of very thin RuO_2 nanowire along the TiO_2 (110) direction as observed from the deposition of RuO_2 on TiO_2(110) single crystals.[23,36] The formation of a new λ-Ti_3O_5 phase (1.4 ~ 2.8 wt%) was clearly observed in all xRuTi heterostructure samples. Based on complementary studies described below, we determined that the appearance of this phase was related to our synthesis method used for the deposition of RuO_2 on TiO_2. This phenomenon has not been observed previously on neither RuO_2/anatase-TiO_2, RuO_2/rutile-TiO_2 nor Ru-doped TiO_2 systems.[12-15,21,31-33,35]

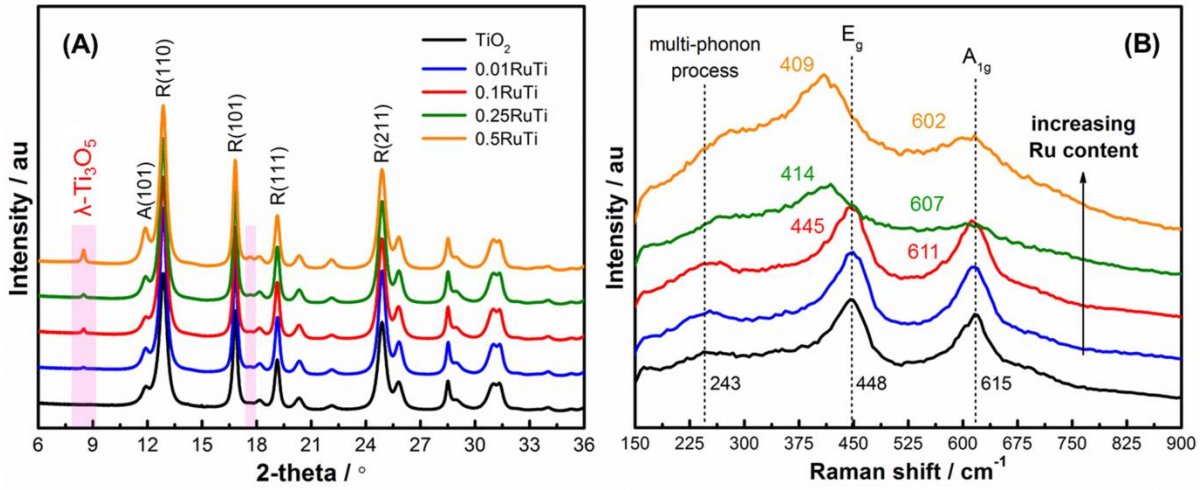

Figure 2. (A) SXPD patterns and (B) Raman spectra of TiO_2 NRs and xRuTi series.

The Raman spectra for different Ru loadings are displayed in **Figure 2B**, where two intense features of tetragonal rutile TiO_2 (space group D_{4h}^{14}) at 448 and 615 cm^{-1} were assigned to E_g (planar O-O vibration) and A_{1g} (Ti-O stretch) modes, respectively, accompanied with a anomalously broad band at 243 cm^{-1} corresponding to the multiple phonon scattering process.[37,38] No characteristic modes of anatase with D_{4h}^{19} space group was found at 145 cm^{-1} (E_g), 198 cm^{-1} (E_g), 398 cm^{-1} (B_{1g}), 518 cm^{-1} (A_{1g}) and 640 cm^{-1} (B_{1g}).[37] Four Raman-active modes of RuO_2 corresponding to B_{2g} (165 cm^{-1}), E_g (528 cm^{-1}), A_{1g} (646 cm^{-1}), and B_{2g} (716 cm^{-1})[35] were not observed for all xRuTi heterostructured materials. More importantly, increasing RuO_2 content up to 0.1, 0.25 and 0.5 wt% resulted in the substantial red-shift and broadening of both E_g to 445, 414 and 409 cm^{-1}, and A_{1g} to 611, 607 and 602 cm^{-1}, respectively. It has been established that the Raman line shape, intensity and position are strongly impacted by the phonon confinement effect, lattice strain, defects, crystallite shape and size.[38-40] Herein, such red shifts of A_{1g} might be attributed to the lattice distortion of TiO_2 meanwhile the shifts in E_g obviously indicate the alteration in oxygen stoichiometry or the higher concentration of oxygen vacancy defects in 0.25RuTi and 0.5RuTi compared to others. The Schottky heterojunction at the interface between RuO_2 and TiO_2 increases the

population of oxygen vacancies, leading to significant charge transfer from TiO_2 to RuO_2 and facilitation of the photoreaction.[41] Such oxygen vacancies are preferential adsorption sites for methanol and water dissociation on TiO_2(110) surface.[22,42,43] Owing to identical surface termination, this deduction should also be applicable for RuO_2/TiO_2 heterostructures and Wei *et al.*[22] found that the oxygen vacancy led to more electrons on the two Ru sites surrounding the oxygen vacancy, making these sites more active for catalytic reactions.[22,44] However, excess quantity of such defects is detrimental to the photoactivity since they become the recombination centers and intensively trapped valence-band holes, reducing the charge density and retarding the separation of charge carriers, and hence, diminishing the photoactivity.

Table 2. Rietveld refinement from SXPD.

Samples	Rutile phase				Anatase phase				λ-Ti_3O_5	
	W_R / % [a]	*a* / Å	*c* / Å	D_R / nm [b]	W_A / % [a]	*a* / Å	*c* / Å	D_A / nm [b]	W_λ / % [a]	D_λ / nm [b]
TiO_2	91.3	4.607(3)	2.959(9)	14	8.7	3.784(9)	9.457(2)	5	-	-
0.01RuTi	91.2	4.604(9)	2.958(1)	16	7.3	3.790(9)	9.469(2)	6	1.5	9
0.1RuTi	89.8	4.608(5)	2.959(4)	15	8.5	3.790(3)	9.426(6)	5	1.7	16
0.25RuTi	91.7	4.605(3)	2.958(9)	16	6.9	3.789(6)	9.495(1)	6	1.4	16
0.5RuTi	86.8	4.605(1)	2.958(9)	14	10.5	3.791(4)	9.507(7)	6	2.8	17

[a] W_R, W_A, W_λ – Weight percentage of rutile, anatase and λ-Ti_3O_5, respectively.

[b] D_R, D_A, D_λ - Crystallite size of rutile, anatase and λ-Ti_3O_5, respectively.

The possible role of λ-Ti_3O_5 in the photocatalytic enhancement of TiO_2 based catalysts is still controversial. A phase transition between different polymorphs of Ti_3O_5, *i.e.* γ- to β-phase, λ- to β-phase, α- to β-phase, γ- to δ-phase, easily happens under thermal treatment or

light irradiation.[45,46] λ-Ti_3O_5 exhibited a reversible light-induced metal-to-semiconductor phase transition between black metallic λ-Ti_3O_5 to brown semiconducting β-Ti_3O_5 at room temperature.[45] To understand the effect of the appearance of this new phase, a TiO_2 sample was prepared by using identical impregnation method without addition of the ruthenium precursor. SXPD pattern in **Figure S5** (Supporting Information) show the existence of λ-Ti_3O_5 phase along with anatase and rutile TiO_2. Hence, we can exclude the formation of λ-Ti_3O_5 due to the incorporation of RuO_2 and that it was formed as a result of preparation conditions. The H_2 evolution activity over treated TiO_2 was measured under the irradiation of UV-visible light (**Figure S5C**). It is apparent that the emerging λ-Ti_3O_5 is detrimental to water splitting reaction while RuO_2 addition dramatically promotes the H_2 production.

Changes in the electronic configuration of TiO_2 NRs upon RuO_2 deposition *via* the formation of surface defects and changes in the chemical environment were probed by X-ray photoelectron spectroscopy. The Ti 2p + Ru 3d, C 1s + Ru 3d and O 1s core level XPS spectra of bare TiO_2 NRs and representative 0.1RuTi heterostructure, the best photocatalyst, are illustrated in **Figure 3**. The complete removal of chlorine by rinsing and subsequent annealing was confirmed by the absence of Cl $2p_{3/2}$ and Cl $2p_{1/2}$ peaks (not shown here). The doublet Ti $2p_{3/2}$ and Ti $2p_{1/2}$ located at 458.7 and 464.4 eV, respectively, is characteristic of the Ti^{4+} state in bare TiO_2 NRs (**Figure 3A**). The addition of 0.1 wt% RuO_2 to TiO_2 induced electronic perturbations *via* a substantial shift of Ti 2p doublet towards lower binding energy (Δ_{BE} = 0.5 eV). Such a blue shift could be associated with the upward band bending at the interface of the RuO_2-TiO_2 heterojunction[21,22] and the formation of lower oxidation state of titanium species, *i.e.* Ti^{3+}. The surface core-level shifts reflect the excess charge at the surface layer of metal atoms due to the reduced coordination.[42] A downward shift of Δ_{BE} = 0.4 eV was also detected in the O 1s spectra (**Figure 3B**) which are consistent with Raman results

discussed above. The unparallel shift of both Ti 2p and O 1s confirms the interfacial reaction between RuO_2 and TiO_2, forming Ti-O-Ru bonds.[35] The presence of ruthenium was clearly confirmed by a broad band representative of Ru $3d_{5/2}$ peak located at 279 - 282 eV as reported in C 1s + Ru 3d core level spectra in **Figure 3C** whereas the $3d_{3/2}$ doublet was superimposed by C 1s feature from carbonaceous impurities and carbonate species. The broad and weak spectrum in the inset indicates the formation of mixtures of Ru^0 and oxidized Ru^{n+} species ($n = 2 \sim 4$).[8,10,11,16,21,35] Due to the intrinsic submetallic property of RuO_2,[8-11,21,31,33-35] these highly dispersed ruthenium species behave as quasi metallic contact materials to enhance both the conductivity and transfer of photoinduced holes from TiO_2 valence band, further facilitating the charge separation, so that the electrons freely migrate from the conduction band of TiO_2, reducing the protons and/or water to generate gaseous H_2.

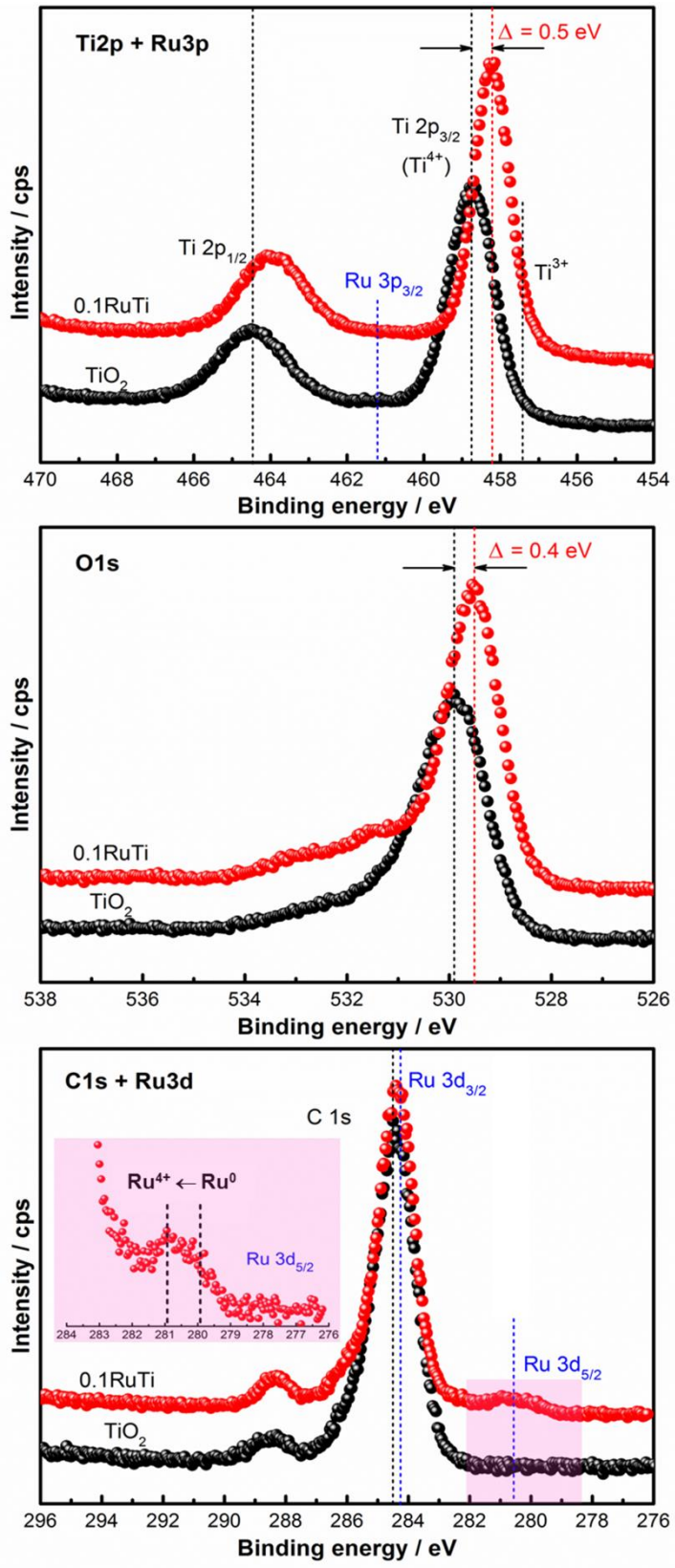

Figure 3. High resolution core-level XPS spectra of TiO_2 and 0.1RuTi: Ti 2p + Ru 3p, O 1s, and C 1s + Ru 3d.

The local geometry of the prepared materials was further studied by electron microscopy. SEM images in **Figure S6A** and **B** (Supporting Information) shows that our pure TiO_2 NRs were uniform nanorods aggregated in three-dimensional (3D) microsphere-like morphology. High-resolution TEM micrograph depicted in **Figure S6C** (Supporting Information) reveals that the highly crystalline rods had a rather constant diameter of about 5-10 nm and the length can be larger than several hundred nm. The well-resolved lattice fringe at 3.25 Å reveals that the highly crystalline NRs were grown along the [110] direction. After depositing 0.1 wt% RuO_2 onto the TiO_2 nanorods, the *d*-spacing of 3.25 Å corresponding to the preferred exposure of {110}-type planes of highly single-crystalline rutile structure was maintained (consistent with the FFT pattern in the inset) and the surface of TiO_2 rods becomes more heterogeneous (**Figure 4A**). It is very difficult to recognize and identify the lattice fringes of RuO_2 by HR-TEM mode stemming from lattice matching between rutile-like RuO_2 and rutile TiO_2, ultrafine particles and small loading amounts. Herein, the high angle annular dark field (HAADF) STEM image in **Figure 4B** indicates that the surface of the rod is rougher than TiO_2 NRs only (**Figure S6D**, Supporting Information) and in some specific regions, 1 ~ 2 nm nanodots (even smaller) were sparsely decorated onto primary TiO_2 NRs. The small nanoparticles are most likely a small fraction of sintered RuO_2. The EDX spectrum in the inset confirmed the presence of Ti, O and Ru signals. However, the microstructure of the rod surface before and after loading RuO_2 in **Figure S7** (Supporting Information) obviously indicates an increase in surface roughness as well as the breakage into smaller fraction of rods. The structural analysis in **Figure S8** (Supporting Information) visually revealed an obvious difference in the lattice fringes of TiO_2 NRs before and after loading RuO_2. Combining several factors, the heteroepitaxial growth of rutile RuO_2 along rutile TiO_2 NRs is proposed to occur because the lattice constants are almost identical. However, if the thickness of epitaxial layers or wires is too thin, approximately few atomic or sub-nanometer level, they

may not be observed microscopically. Similar behavior was studied by our group and other groups.[12,13,23,36] We have observed in previous fundamental studies[23,36] the growth of 1D wire-like rows of RuO_x extending along the <001> direction of TiO_2(110) single crystals in which each RuO_2 wire with an apparent width of few angstrom covered three rows of TiO_2(110) rows. Elevating temperature under UHV pressure resulted in the disappearance of RuO_x wires and the formation of Ru nanoparticles. The RuO_2/TiO_2(110) surfaces were much more reactive towards CO oxidation, ethanol photo-oxidation and water dissociation than TiO_2(110) or RuO_2(110) due to the enhanced charge separation at the RuO_2-TiO_2 interface.[23,36,47]

The distribution of RuO_2 on TiO_2 NRs is obviously different from that over bulk TiO_2 particles where the presence of abundant round-shaped RuO_2 nanoparticles with an average diameter of 2-3 nm was extensively found in **Figure 4C**. One can clearly see a well-resolved fringe spacing of 3.25 Å that is indexed to (110) crystallographic plane of rutile TiO_2 and the inset FFT pattern indicates the single-crystalline nature of the support. At high coverage of RuO_2 nanoclusters whose *d*-spacing of 2.6 Å corresponds to (101) plane on the surface of bulk-like crystalline titania (**Figure 4D**), it resulted in much lower performance towards light-activated H_2 production over bulk supported catalysts.

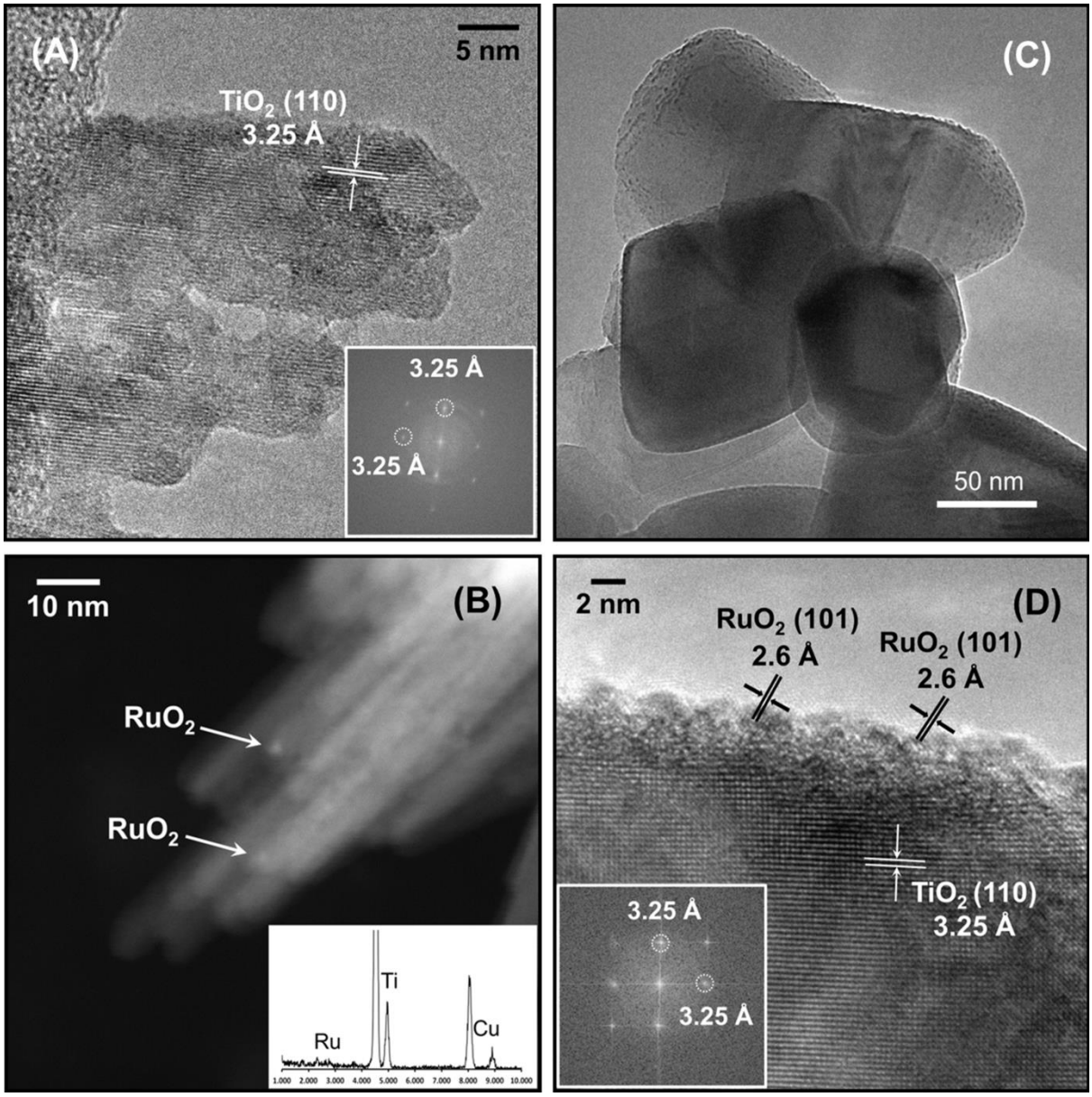

Figure 4. (A, B) HR-TEM and HAADF-STEM micrograph of 0.1 wt% RuO_2 onto TiO_2 NRs, respectively; (C, D) HR-TEM images of 0.1% RuO_2 loaded on bulk TiO_2 particles. The insets of A and D are corresponding FFT patterns and the inset of B is EDX spectrum.

We carried out DFT studies to understand the electronic band structure of the heterojunction nanocomposites which strongly affects the photocatalytic water splitting performance. In **Figure 5A**, we show the density of states (DOS) of the full-relaxed (3x6) surface model for the system RuO_2 nanowire (RuO_2^w) supported on TiO_2(110) that we have

reported previously.[23] The large band below 2 eV is mainly related to O 2*p* levels from both oxides. The states just below Fermi level consists primarily of Ru 4*d* states, with small contribution from the O 2*p* states of the oxygen atoms of RuO_2. Therefore, the states observed in the UPS spectra just below the Fermi level are related to the supported RuO_2, mainly from metallic ruthenium states. The states above the Fermi level consists firstly of Ru 4*d* levels and above 0.2-0.3 eV the 3*d* states of titanium appear strongly. Therefore *d-d* transitions between 4*d* states of the supported ruthenia along with 3*d* states of titania support may take place in the heterostructure with an abrupt interface. The total DOS is consistent with the experimental ultraviolet photoelectron spectroscopy valence band (UPS-VB) spectra shown in **Figure 5B**. The UPS-VB spectra of TiO_2 NRs and $0.1RuO_2/TiO_2$ heterostructure were measured in which two features centered at 4.8 eV and 6.6 eV are associated with the typical O *2p*-Ti *3d* structure of TiO_2. The position of the valence band maximum (VBM) for TiO_2 NRs locates at 1.87 eV (estimated by linear extrapolation), which is characteristic of a VB DOS of rutile TiO_2. It should be noted that the RuO_2 deposition induces a blue-shift to 1.75 eV of VB edge maximum energy and a tailing feature toward the vacuum level at ~ -0.6 eV confirms the submetallic character of RuO_2. Such energy shifts in VBM and XPS core levels demonstrate the band gap narrowing, band bending, and the formation of strong built-in electric field at the heterojunction at the interface that was previously reported by DFT calculation,[22] resulting in efficient separation of charge carriers during the photocatalytic process.

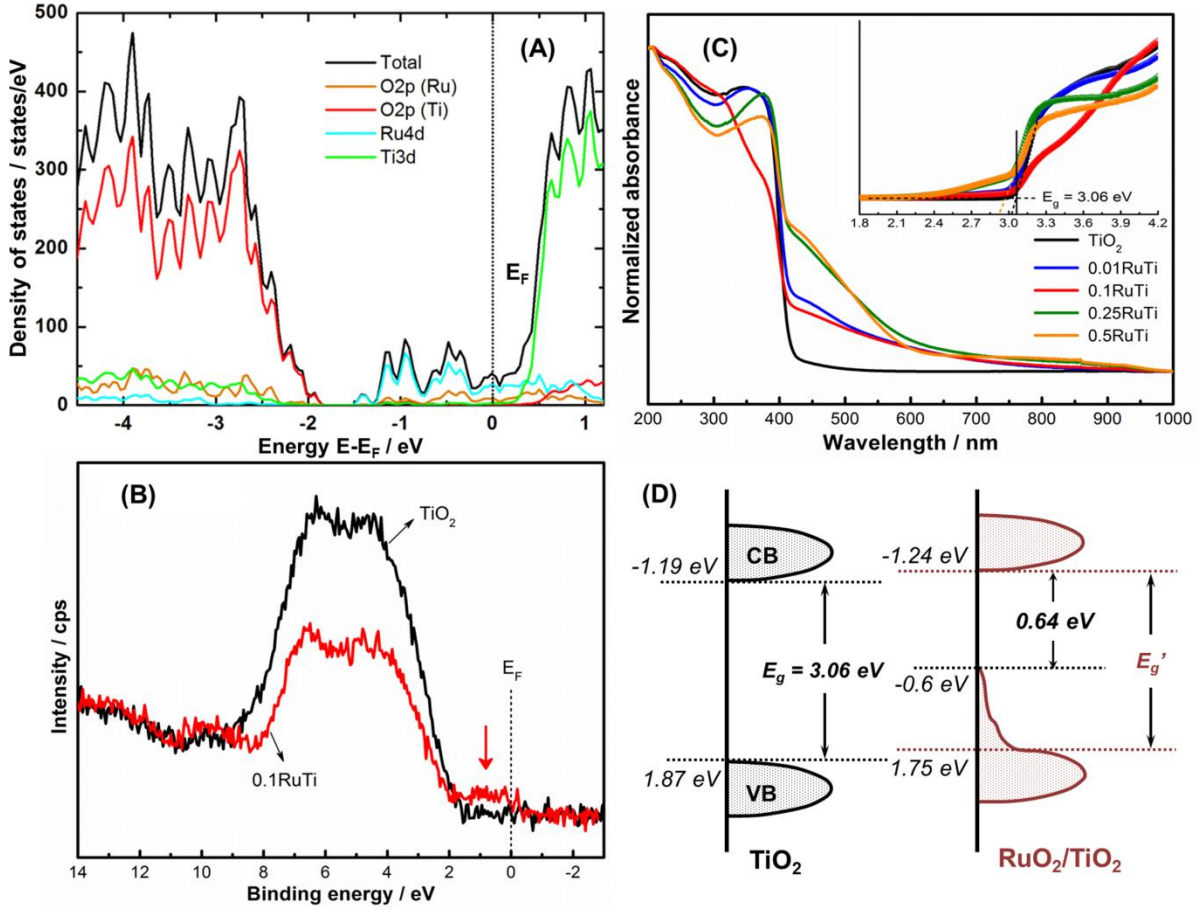

Figure 5. (A) Total and partial density of states (DOS) on O, Ru and Ti atoms of $RuO_2/TiO_2(110)$ system (the Fermi level E_F is set to energy zero); (B) experimental UPS-VB spectra of TiO_2 NRs and $0.1RuO_2/TiO_2$ heterostructure; (C) UV-Vis diffused absorption spectra of TiO_2 and xRuTi series; and (D) representative band diagram of TiO_2 and RuO_2/TiO_2 heterostructure. The inset of (C) is the Tauc's plot for direct band gap determination.

Figure 5C shows the UV-Vis diffused absorption spectra of TiO_2 NRs and xRuTi heterostructures with various RuO_2 contents. The absorption onset of bare TiO_2 NRs located at *ca.* 410 nm due to O 2*p*-Ti 3*d* transitions. The edges were slightly red-shifted toward the longer wavelength region with increasing RuO_2 loading amounts, indicating the narrowing of the band gap. Consequently, the band gaps (E_g) determined by Tauc's plot in the inset are

summarized in **Table 1**. A gradual reduction of the band gap from 3.06 eV to 2.93 eV is observed with further increasing RuO_2 contents up to 0.5 wt%. It is interesting to note that strong, broad absorption bands and long tails across the whole visible regime was observed in all oxide heterostructures which might be associated with several factors, *i.e.* the transition between Ti 3*d* and Ru 4*d*, band transition of RuO_2 itself, defect level states, and/or the localized surface plasmon resonance mediated absorption of RuO_2 nanodots.[10,11] Two types of band-edge transition of RuO_2 have been reported: (*i*) O 2*p*- Ru 4*d* interband transition, resulting in an optical absorption at shorter wavelength range (up to 2.1 eV, ~ 580 nm); and (*ii*) *d*-*d* intraband transition between partially filled and unfilled Ru 4*d* orbitals or free carrier absorptions, giving an electronic band at 1.5-1.9 eV (~ 800 – 650 nm).[10,48] And the proximity of surface plasmon and interband transition energies results in a damping of surface plasmon by interband electron excitations, thus reducing the surface plasmon local field.[49] In the present study, it might be conclusive that the effect of Ru 4*d*-Ti 3*d* transition (or hybridized state) and O 2*p*-Ru 4*d* interband transition of RuO_2 is more pronounced than the *d*-*d* intraband transition of RuO_2, exhibiting significant enhancement in visible light absorption, therefore enabling RuO_2/TiO_2 heterostructure to efficiently produce H_2 as compared to blank TiO_2. Especially, an increase in visible absorption is coincident with a decrease in UV region; and the O 2*p*-Ti 3*d* direct transition in range of 200-400 nm for 0.1RuTi sample was distinct from others, possibly stemming from the stronger local electronic distortion in TiO_2 by RuO_2 and faster interfacial charge transfer from TiO_2 to RuO_2. Both band gap narrowing and enhanced absorption features in visible regime notably confirm that all rod-like RuO_2/TiO_2 heterostructures are highly efficient visible-light-responsive photocatalysts.

On the contrary, very poor visible-light absorption behavior was observed when loading 0.1 wt% RuO_2 onto bulk TiO_2 particles as indicated in **Figure S9** (Supporting Information). It is interesting to note that the an absorption tail towards visible light region up to 480 nm were

observed on rutile TiO_2 NRs which did not happen with bulk rutile TiO_2. Recently, Li *et al.*[30] reported similar visible light absorption over sub-10nm rutile TiO_2 NPs compared to bulk-like or larger-grain-size rutile TiO_2. A slightly increased absorbance in the range of 700-1000 nm is more visible than that ranging from 400 to 550 nm, accounting for the dominance of partially filled and unfilled Ru 4*d* electronic bands (*d*-*d* intraband transition). That contributes to extremely lower UV activity and almost no visible-light-responsive activity (not shown here) of bulk TiO_2 and 0.1RuTi_p material. The photoluminescence spectroscopy (**Figure S10**, Supporting Information) was additionally performed to understand the efficiency of charge carrier trapping, migration, transfer and separation. PL peak intensity of xRuTi heterostructure relatively decreases with increasing RuO_2 amounts, implying the suppression of electron-hole recombination rate that favors the higher photocatalytic activity. It can be seen that although the loading beyond 0.1 % exhibits lower recombination rate, worse H_2 production performance was obtained possibly due to the dominance of light shielding effect and abundance of oxygen vacancy defects as mentioned above that remarkably inhibit the performance.

Gathering the experimental data of E_g and VBM of 0.1RuTi nanocomposite, a possible band level alignment diagram at the interface is schematically shown in **Figure 5D**. The formation of a heterojunction at the RuO_2-TiO_2 interface, band gap narrowing, and upward band bending at the interface effectively promote the separation of photoinduced electrons and holes, leading to an increase in photocatalytic H_2 evolution.

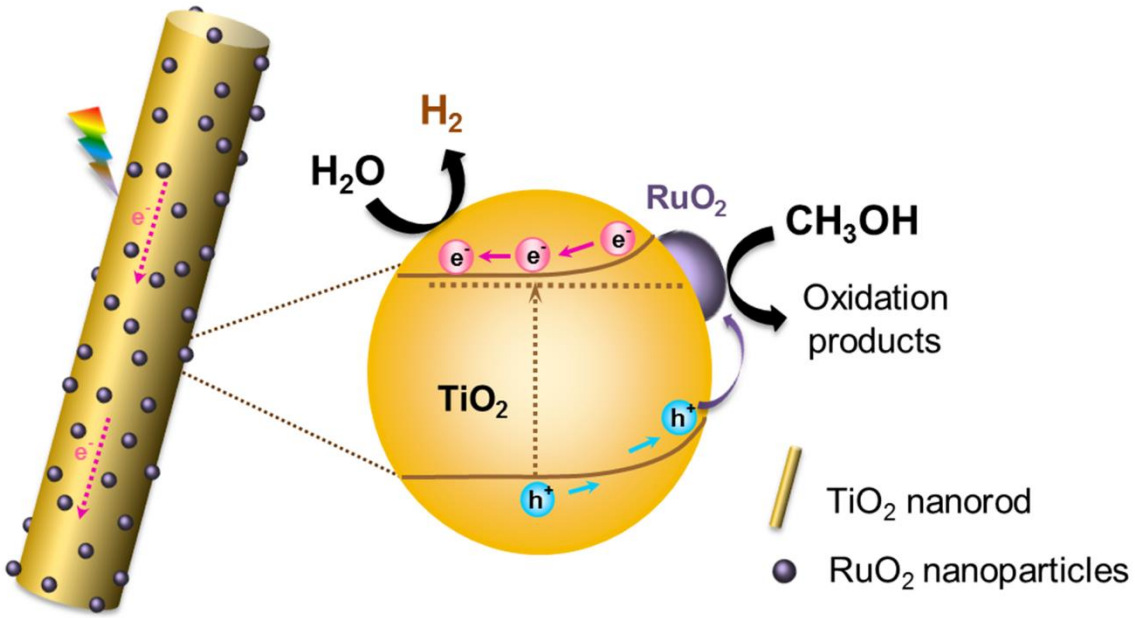

Scheme 1. Schematic illustration of proposed upward band bending-involved charge transfer pathway of RuO_2/TiO_2 heterojunction nanocomposite to produce H_2 under visible light irradiation.

Scheme 1 illustrates the proposed charge transfer pathway over RuO_2/TiO_2 heterostructures to produce H_2. By this way, it favors the dynamic transfer of electrons and holes from TiO_2 to RuO_2 *via* an intimate contact due to higher work function of RuO_2,[19,21,35] subsequently reacting with protons, water and methanol. The photoinduced holes from VB of TiO_2 NRs are irreversibly scavenged by methanol to produce various oxidation intermediates and products such as $^{\bullet}OH$ radical, $^{\bullet}CH_2OH$, HCHO, HCOOH and CO_2.[31,35,50] Meanwhile, the photogenerated electrons simultaneously reduce the protons and water to generate H_2 gas. These reactions proceed competitively with the recombination of electron-hole pairs. Herein, RuO_2 efficiently stabilizes the holes and creates the heterojunction or a Schottky barrier at the heterointerface between RuO_2 and TiO_2,[3,6,35] hindering the charge carrier recombination and consequently, enhancing the H_2 evolution. Because Ru is more electronegative than Ti (2.2 *vs.* 1.54), the strong accumulation of electron density at the interface creates a strong internal

electric field between the interface and its adjacent TiO_2 layer.[22] The distribution of electric field is inhomogeneous, directly relating to the gradient of the space charge or band bending potential.[11] Thereby, the photoinduced electron-hole pairs adjacent to the interface are separated more efficiently than those generated on pure TiO_2 surfaces. The transport, transfer and separation of charge carriers are promoted in the presence of RuO_2 and the photocatalytic H_2 production activity is prominently enhanced. The unique nanoparticle-nanorod geometry also contributes to the excellent efficiency due to the favorable vectorial electron transport within the 1D TiO_2 structure. Additionally, the trapping centers involving Ti^{3+} sites as the electron scavengers and the oxygen vacancies as hole trapping centers are crucial in enhancing the photo-oxidation of methanol and consequently, hydrogen production. It is conclusive that the optimized RuO_2 concentration is a crucial factor in accounting for the photocatalytic properties *via* properly manipulating geometry, levels of defects and interfacial electronic alignment.

CONCLUSION

We have successfully developed heterojunction nanocomposites by loading miniscule quantities of RuO_2 onto 1D rutile TiO_2 NRs and these materials exhibited superior visible-light-driven H_2 generation activity. Our study proved that the unique geometry, abundance of surface defects, band gap narrowing, visible photoresponse and favorable upward band bending at the heterointerface significantly facilitate the charge transfer and separation of photogenerated electron-hole pairs. 0.1 wt% of RuO_2 was the optimal loading amount to achieve the highest H_2 evolved rate. The comparison with bulk-like support and Pt counterpart obviously demonstrates that the rod-like heterostructures is extremely crucial to visible-light-responsive activity. In perspective, this study provides a simple, scalable and cost-effective approach to produce efficient heterogeneous photocatalysts for solar hydrogen production from water.

ASSOCIATED CONTENT

Supporting Information. Includes description of SEM and PL techniques, detailed experiment of H2 production; supporting figures (Figure S1 to S10) of time profiles and H2 production rate of Ru and Pt-based heterostructures under either UV or visible light irradiation, Rietveld refinement, SEM/HR-TEM/HAADF-STEM images, UV-Vis-DRS and Tauc's plot and PL spectra.

AUTHOR INFORMATION

Corresponding Author

* rodrigez@bnl.gov (J. A. Rodriguez), djs@bnl.gov (D. J. Stacchiola)

Notes

The authors declare no competing financial interest.

ACKNOWLEDGEMENT

The research was performed at Brookhaven National Laboratory, supported by the U.S. Department of Energy, Office of Science, Office of Basic Energy Sciences, and Catalysis Science Program under contract No. DE-SC0012704. This work used resources of the Center for Functional Nanomaterials (CFN) and Advanced Photon Science - Argonne National Laboratory (APS-ANL) which are DOE Office of Science User Facilities. Dr. Viet Hung Pham (CFN) is acknowledged for Raman analysis. J.L. is Serra Húnter Fellow and is grateful to ENE2014-61715-EXP and ICREA Academia program.

REFERENCES

(1) Kudo, A.; Miseki, Y. Heterogeneous Photocatalyst Materials for Water Splitting. *Chem. Soc. Rev.* **2009**, *38*, 253-278.

(2) Yang, J.; Wang, D.; Han, H.; Li, C. Role of Cocatalysts in Photocatalysis and Photoelectrocatalysis. *Acc. Chem. Res.* **2013**, *46*, 1900-1909.

(3) Yuan, Y.-P.; Ruan, L.-W.; Barber, J.; Loo, S.C.J.; Xue, C. Hetero-Nanostructured Suspended Photocatalysts for Solar-To-Fuel Conversion. *Energy Environ. Sci.* **2014**, *7*, 3934-3951.

(4) Chen, X.; Mao, S.S. Titanium Dioxide Nanomaterials: Synthesis, Properties, Modifications, and Applications. *Chem. Rev.* **2007**, *107*, 2891-2959.

(5) Habisreutinger, S.N.; Schmidt-Mende, L.; Stolarczyk, J.K. Photocatalytic Reduction of CO_2 on TiO_2 and Other Semiconductors. *Angew. Chem. Int. Ed.* **2013**, *52*, 7372-7408.

(6) Dahl, M.; Liu, Y.; Yin, Y. Composite Titanium Dioxide Nanomaterials. *Chem. Rev.* **2014**, *114*, 9853-9889.

(7) Kubacka, A.; Fernández-García, M.; Colón, G. Advanced Nanoarchitectures for Solar Photocatalytic Applications. *Chem. Rev.* **2012**, *112*, 1555-1614.

(8) Over, H. Surface Chemistry of Ruthenium Dioxide in Heterogeneous Catalysis and Electrocatalysis: From Fundamental to Applied Research. *Chem. Rev.* **2012**, *112*, 3356-3426.

(9) de Almeida, J.S.; Ahuja, R. Electronic and Optical Properties of RuO_2 and IrO_2. *Phys. Rev.* **2006**, *73*, 165102.

(10) Bang, S.; Lee, S.; Park, T.; Ko, Y.; Shin, S.; Yim, S.-Y.; Seo, H.; Jeon, H. Dual Optical Functionality of Local Surface Plasmon Resonance for RuO_2 Nanoparticle-

ZnO Nanorod Hybrids Grown by Atomic Layer Deposition. *J. Mater. Chem.* **2012**, *22*, 14141-14148.

(11) Uddin, Md. T.; Nicolas, Y.; Olivier, C.; Servant, L.; Toupance, T.; Li, S.; Klein, A.; Jaegermann, W. Improved Photocatalytic Activity in RuO_2-ZnO Nanoparticulate Heterostructures due to Inhomogeneous Space Charge Effects. *Phys. Chem. Chem. Phys.* **2015**, *17*, 5090-5102.

(12) Cheng, K.-W.; Lin, Y.-T.; Chen, C.-Y.; Hsiung, C.-P.; Gan, J.-Y.; Yeh, J.-W.; Hsieh, C.-H.; Chou, L.-J.. In Situ Epitaxial Growth of TiO_2 on RuO_2 Nanorods with Reactive Sputtering. *Appl. Phys. Lett.* **2006**, *88*, 043115.

(13) Chueh, Y.-L.; Hsieh, C.-H.; Chang, M.-T.; Chou, L.-J.; Lao, C.S.; Song, J.H.; Gan, J.-Y.; Wang, Z.L. RuO_2 Nanowires and RuO_2/TiO_2 Core/Shell Nanowires. From Synthesis to Mechanical, Optical, Electrical, and Photoconductive Properties. *Adv. Mater.* **2007**, *19*, 143-149.

(14) Seki, K. Development of RuO_2/Rutile-TiO_2 catalysts for Industrial HCl Oxidation Process. *Catal. Surv. Asia* **2010**, *14*, 168-175.

(15) Xiang, G.; Shi, X.; Wu, Y.; Zhuang, J.; Wang, X. Size Effects in Atomic-Level Epitaxial Redistribution Process of RuO_2 over TiO_2. *Sci. Rep.* **2012**, *2*, 801.

(16) Jiao, Y.; Jiang, H.; Chen, F. RuO_2/TiO_2/Pt Ternary Photocatalysts with Epitaxial Heterojunction and Their Application in CO Oxidation. *ACS Catal.* **2014**, *4*, 2249-2257.

(17) Lin, Q.; Huang, Y.; Wang, Y.; Li, L.; Liu, X.Y.; Lv, F.; Wang, A.; Li, W.-C.; Zhang, T. RuO_2/rutile-TiO_2: a superior catalyst for N_2Odecomposition. *J. Mater. Chem. A* **2014**, *2*, 5178-5181.

(18) Blondeel, G.; Harriman, A.; Porter, G.; Urwin, D.; Kiwi, J. Design, Preparation and Characterization of Ruthenium Dioxide/Titanium Dioxide Catalytic Surfaces Active in Photooxidation of Water. *J. Phys. Chem.* **1983**, *87*, 2629-2636.

(19) Sakata, T.; Hashimoto, K.; Kawai, T. Catalytic Properties of Ruthenium Oxide on n-Type Semiconductors under Illumination. *J. Phys. Chem.* **1984**, *88*, 5214-5221.

(20) Mills, A.; Duckmanton, P.A.; Reglinski, J. A Simple, Novel Method for Preparing an Effective Water Oxidation Catalyst. *Chem. Commun.* **2010**, *46*, 2397-2398.

(21) Uddin, Md.T.; Babot, O.; Thomas, L.; Olivier, C.; Redaelli, M.; D'Arienzo, M.; Morazzoni, F.; Jaegermann, W.; Rockstroh, N.; Junge, H.; Toupance, T. New Insights into the Photocatalytic Properties of RuO_2/TiO_2 Mesoporous Heterostructures for Hydrogen Production and Organic Pollutant Photodecomposition. *J. Phys. Chem. C* **2015**, *119*, 7006-7015.

(22) Wei, W.; Dai, Y.; Huang, B.; Li, X.; Nägele, F.; Over, H.; Whangbo, M.-H.; Jacob, T. Density Functional Characterization of the Electronic Structures and Band Bending of Rutile RuO_2/TiO_2(110) Heterostructures. *J. Phys. Chem. C* **2015**, *119*, 12394-12399.

(23) Yang, F.; Kundu, S.; Vidal, A.B.; Graciani, J.; Ramírez, P.J.;Senanayake, S.D.; Stacchiola, D.; Evans, J.; Liu, P.; Sanz, J.F.; Rodriguez, J.A. Determining the Behavior of RuO_x Nanoparticles in Mixed-Metal Oxides: Structural and Catalytic

Properties of $RuO_2/TiO_2(110)$ Surfaces. *Angew. Chem., Int. Ed.* **2011**, *50*, 10198-10202.

(24) Perdew, J. P.; Wang, Y. Accurate and Simple Analytic Representation of the Electron-Gas Correlation Energy. *Phys. Rev. B* **1992**, *45*, 13244-13249.

(25) Kresse, G.; Joubert, D. From Ultrasoft Pseudopotentials to the Projector Augmented-Wave Method. *Phys. Rev. B* **1999**, *59*, 1758-1775.

(26) Kresse, G.; Hafner, J. *Ab Initio* Molecular Dynamics for Liquid Metals. *Phys. Rev. B* **1993**, *47*, 558-561.

(27) Kresse, G.; Furthmüller, J. Efficiency of *Ab-Initio* Total Energy Calculations for Metals and Semiconductors using a Plane-Wave Basis Set. *J. Comput. Mater. Sci.* **1996**, *6,* 15-50.

(28) Dudarev, S. L.; Botton, G. A.; Savrasov, S. Y.; Humphreys, C. J.; Sutton, A. P. Electron-Energy-Loss Spectra and the Structural Stability of Nickel Oxide: An LSDA+U Study. *Phys. Rev. B* **1998**, *57*, 1505-1509.

(29) Park, J. B.; Graciani, J.; Evans, J.; Stacchiola, D.; Senanayake, S. D.; Barrio, L.; Liu, P.; Sanz, J. F.; Hrbek, J.; Rodriguez, J. A. Gold, Copper, and Platinum Nanoparticles Dispersed on $CeO_x/TiO_2(110)$ Surfaces: High Water-Gas Shift Activity and the Nature of the Mixed-Metal Oxide at the Nanometer Level. *J. Am. Chem. Soc.* **2010**, *132*, 356-363.

(30) Li, L.; Yan, J.; Wang, T.; Zhao, Z.-J.; Zhang, J.; Gong, J.; Guan, N. Sub-10 nm Rutile Titanium Dioxide Nanoparticles for Efficient Visible-Light-Driven Photocatalytic Hydrogen Production. *Nat. Commun.* **2015**, *6*, 5881.

(31) Ismail, A.A.; Robben, L.; Bahnemann, D.W. Study of the Efficiency of UV and Visible-Light Photocatalytic Oxidation of Methanol on Mesoporous RuO_2-TiO_2 Nanocomposites. *Chem. Phys. Chem.* **2011**, *12*, 982-991.

(32) Ovoshchnikov, D.S.; Donoeva, B.G.; Golovko, V.B. Visible-Light-Driven Aerobic Oxidation of Amines to Nitriles over Hydrous Ruthenium Oxide Supported on TiO_2. *ACS Catal.* **2015**, *5*, 34-38.

(33) Amama, P.B.; Itoh, K.; Murabayashi, M. Effect of RuO_2 Deposition on the Activity of TiO_2: Photocatalytic Oxidation of Trichloroethylene in Aqueous Phase. *J. Mater. Sci.* **2004**, *39*, 4349-4351.

(34) Lin, F.; Zhang, Y.; Wang, L.; Zhang, Y.; Wang, D.; Yang, M.; Yang, J.; Zhang, B.; Jiang, Z.; Li, C. Highly Efficient Photocatalytic Oxidation of Sulfur-Containing Organic Compounds and Dyes on TiO_2 with Dual Cocatalysts Pt and RuO_2. *Appl. Catal. B: Environ.* **2012**, *127*, 363-370.

(35) Uddin, Md.T.; Nicolas, Y.; Olivier, C.; Toupance, T.; Müller, M.M.; Kleebe, H.-J.; Rachut, K.; Ziegler, J.; Llein, A.; Jaegermann, W. Preparation of RuO_2/TiO_2 Mesoporous Heterostructures and Rationalization of Their Enhanced Photocatalytic Properties by Band Alignment Investigations. *J. Phys. Chem. C* **2013**, *117*, 22098-22110.

(36) Kundu, S.; Vidal, A.B.; Yang, F.; Ramírez, P.J.; Senanayake, S.D.; Stacchiola, D.; Evans, J.; Liu, P.; Sanz, J.F.; Rodriguez, J.A. Special Chemical Properties of RuO_x Nanowires in RuO_x/TiO_2(110): Dissociation of Water and Hydrogen Production. *J. Phys. Chem. C* **2012**, *116*, 4767-4773.

(37) Balachandran, U.; Eror, N.G. Raman Spectra of Titanium Dioxide. *J. Solid State Chem.* **1982**, *42*, 276-282.

(38) Ocaña, M.; Fornés, V.; Ramos, J.V.G.; Serna, C.J., Factors Affecting the Infrared and Raman Spectra of Rutile Powders. *J. Solid State Chem.* **1988**, *75*, 364-372.

(39) Parker, J.C.; Siegel, R.W. Calibration of the Raman Spectrum to the Oxygen Stoichiometry of Nanophase TiO_2. *Appl. Phys. Lett.* **1990**, *57*, 943-945.

(40) Santara, B.; Giri, P.K.; Imakita, K.; Fujii, M. Microscopic Origin of Lattice Contraction and Expansion in Undoped Rutile TiO_2 Nanostructures. *J. Phys. D: Appl. Phys.* **2014**, *47*, 215302.

(41) Badyal, J.P.S.; Lambert, R.M.; Harrison, K.; Riley, C.C.A.; Frost, J.C. Investigation of the SMSI Phenomenon with TiO_2/Ru/SiO_2 Model-Dispersed Catalysts. *J. Catal.* **1991**, *129*, 486-496.

(42) Wendt, S.; Matthiesen, J.; Schaub, R.; Vestergaard, E. K.;Laegsgaard, E.; Besenbacher, F.; Hammer, B. Formation and Splitting of Paired Hydroxyl Groups on Reduced TiO_2(110). *Phys. Rev. Lett.* **2006**, *96*, 066107.

(43) Oviedo, J.; Sánchez-de-Armas, R.; Ángel San Miguel, M.; Sanz, J.F. Methanol and Water Dissociation on TiO_2(110): The Role of Surface Oxygen. *J. Phys. Chem. C* **2008**, *112*, 17737-17740.

(44) Stacchiola, D.J.; Senanayake, S.D.; Liu, P.; Rodriguez, J.A. Fundamental Studies of Well-Defined Surfaces of Mixed-MetalOxides: Special Properties of MO_x/TiO_2(110) {M = V, Ru, Ce, or W}. *Chem. Rev.* **2013**, *113*, 4373-4390.

(45) Ohkoshi, S.; Tsunobuchi, Y.; Matsuda, T.; Hashimoto, K.; Namai, A.; Hakoe, F.; Tokoro, H. External Stimulation-Controllable Heat-Storage Ceramics. *Nat. Chem.* **2010**, *2*, 539.

(46) Tanaka, K.; Nasu, T.; Miyamoto, Y.; Ozaki, N.; Tanaka, S.; Nagata, T.; Hakoe, F.; Yoshikiyo, M.; Nakagawa, K.; Umeta, Y.; Imoto, K.; Tokoro, H.; Namai, A.; Ohkoshi, S. Structural Phase Transition between γ-Ti_3O_5 and δ-Ti_3O_5 by Breaking of a One-Dimensionally Conducting Pathway. *Cryst. Growth Des.* **2015**, *15*, 653-657.

(47) Kundu, S.; Vidal, A. B.; Nadeem, M. A.; Senanayake, S. D.; Idriss, H.; Liu, P.; Rodriguez, J. A.; Stacchiola, D. Ethanol Photoreaction on RuO_x/Ru-Modified TiO_2(110). *J. Phys. Chem. C* **2013**, *117*, 11149-11158.

(48) Tan, H.; Ye, E.Y.; Fan, W.Y. Alumina-Template Synthesis of Fluorescent RuO_2 Nanotubes Derived from $Ru_3(CO)_{12}$ Clusters. *Adv. Mater.* **2006**, *18*, 619-623.

(49) Pustovit, V.N.; Shahbazyan, T.V. Finite-Size Effects in Surface-Enhanced Raman Scattering in Noble-Metal Nanoparticles: A Semiclassical Approach. *J. Opt. Soc. Am. A* **2006**, *23*, 1369-1374.

(50) Schneider, J.; D. W. Bahnemann, D. W. Undesired Role of Sacrificial Reagents in Photocatalysis. *J. Phys. Chem. Lett.* **2013**, *4*, 3479-3483.

TABLE OF CONTENTS AND ABSTRACT GRAPHIC